

Design Optimization of Vortex Generator Array to Delay Pitch-up on Tailless Aircraft

Seonguk Lee* and Chongam Kim*,**
Corresponding author: chongam@snu.ac.kr

* Department of Mechanical and Aerospace Engineering, Seoul National University, Korea
** Institute of Advanced Aerospace Technology, Seoul National University, Korea

Abstract: This paper deals with the design optimization of vortex generators (VGs) to delay the pitch-up on the tailless lambda wing aircraft. The pitch-up is an unstable pitching moment characteristic that the lambda wing aircraft has inherently. From previous studies, it was shown that the pitch-up is caused by the flow separation on the outboard upper wing. In this study, VGs were adopted and optimized to suppress the flow separation on the upper wing with a VG size as small as possible. To enhance the computational efficiency, each VG was presented as a mathematical source-term model, the differentiable BAY model, instead of a fully gridded vortex generator. To analyze the flow characteristics of the parameters defining the VG, four parametric studies were performed; then, gradient-based design optimizations using the discrete adjoint variable method were conducted with five design parameters of the chord length, the height, the incidence angle, the streamwise (x -directional) position, and the spanwise (y -directional) position of the VGs. As a result of the parametric study, the pitching moment coefficient decreased a maximum of 199% from the initial case without VGs under the design condition ($\alpha = 11^\circ$). After carrying out the optimization of the VGs, the region of flow separation was diminished; thus, the pitching moment coefficient decreased over 172% from the initial case while the size of VGs decreased over 42% from the baseline VGs. The slope of the pitching moment coefficient declined and showed more gently up at the design condition than the initial case as well as the case with the baseline VGs.

Keywords: Design Optimization, Vortex Generator, Source Term Model, Pitch-up, Tailless Lambda Wing.

1 Introduction

The tailless lambda wing configuration has high maneuverability and low observability; thus, it has been used for various purposes, such as Unmanned Air Vehicles (UAVs). The 1303 UCAV (Unmanned Combat Air Vehicle) planform, created by the US Air Force Research Laboratory (AFRL) and the Boeing Company, is a typical representative of the lambda wing aircraft. Many experimental and numerical studies [1, 2, 3, 4] have demonstrated that this type of wing has an inherently low longitudinal stability due to, for example, the pitch-up phenomenon, which is an unstable pitching moment characteristic that occurs at a certain range of angle of attack. McParlin *et al.* [3] showed that the pitch-up is due to the flow separation over the outboard wing panel. Ol [4] also demonstrated that the pitch-up results from a loss of suction close to the wing tip and a slight increase in suction near the wing apex.

The Vortex Generator (VG) is known as a very useful and passive flow control device that can prevent the flow separation. It increases the momentum of the boundary layer by making small vortices and efficiently mixing the freestream with the boundary layer, which in turn reduces the flow separation. Since stealth is the crucial design factor of general UAV configuration, VGs can be selectively exploited to avoid any reduction in stealth capability.

From this perspective, the present study focuses on suppressing the pitch-up by installing an array of

VGs to mitigate the flow separation, and further optimizing the VG array to maximize the pitch-up delay while minimizing the size of each VG.

2 Numerical Method

Numerical studies were carried out using a 3-D parallelized incompressible Reynolds-Averaged Navier–Stokes (RANS) solver based on the artificial compressibility method. Third-order MUSCL interpolation was used for high-order accuracy, and Yoon’s LU-SGS scheme [5] was used for time integration. Menter’s $k - \omega$ Shear Stress Transport (SST) model [6] was incorporated for turbulent flow characteristics.

2.1 Model Geometry and Validation

As a target geometry, the same tailless lambda wing geometry of the experiment [7] was adopted for the flow analysis and the design optimization. The lambda wing model has the same planform as that of the 1303 UCAV model, as mentioned earlier [1, 2, 3, 4], but it was slightly modified from the 1303 UCAV configuration. The lambda wing model, shown in Figure 1, has a wing span of 1 m, a mean aerodynamic chord (MAC) of 0.3522 m, a leading edge sweep angle of 47°, a trailing edge crank angle of 30°, and a washout twist angle of 0°. Moment reference point (MRP) is located at 0.3011 m from the apex. The leading edge is round until $\eta = 0.86$ (η is the ratio of y -position to the wing span) from the center of the model in the spanwise direction, and the wing tip and the trailing edge are sharp for a stealth performance. The details of specification of the model are shown in Table 1.

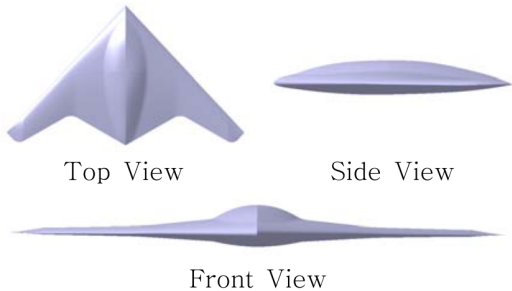


Figure 1: Three views of tailless lambda wing model [7]

Table 1: Specifications of 1303 UCAV model [7]

Wing span	1000 mm
Body center line	590.551 mm
Reference area	0.259 m ²
Mean aerodynamic chord	352.2 mm
Leading edge sweep angle	47°
Moment reference point	301.1 mm (from apex)
Airfoil	NACA 64A210
Twist angle	0°

For flow computation, the grid (Figure 2) was generated in C-H type with multi-blocks, and the grid, which has 10.2 million cells, was selected by a grid refinement test. The flow conditions matched those of the wind tunnel experiment [7]. The freestream velocity is 70 m/s, and the Reynolds number based on the MAC is 1.75×10^6 .

Figure 3 shows the aerodynamic coefficients with respect to the angles of attack and the experimental results [7]. In the experimental results, the lift curve (Figure 3(a)) is linear up to about 10° angle of attack, after which the slope starts to decrease. The present results show good agreement with the experimental results up to 10° and a discrepancy after that angle. In the plot of drag coefficient (Figure 3(a)), the numerical result shows good agreement with the experimental result in the entire range. The pitching moment coefficient, as shown in Figure 3(b), shows an overall trend, such as an increase of the pitching moment after the pitch-up angle ($\sim 5^\circ$) and an increase of the slope after about 10°, which agreed well with the experimental result. However, the numerical result fails to predict the change of the slope between 5° and 9°, or the slope of the region in which pitching moment varies rapidly after 10°.

McParlin *et al.*’s experimental results [3] show that the leading edge separation and the trailing edge separation at the outboard wing panel merged into the larger separation and expanded to the inboard. The upper wing outside the crank was covered entirely with the separated flow, and the lift in that region decreased. Since that region was located behind the MRP, it generated the nose-up moment. While the comparison

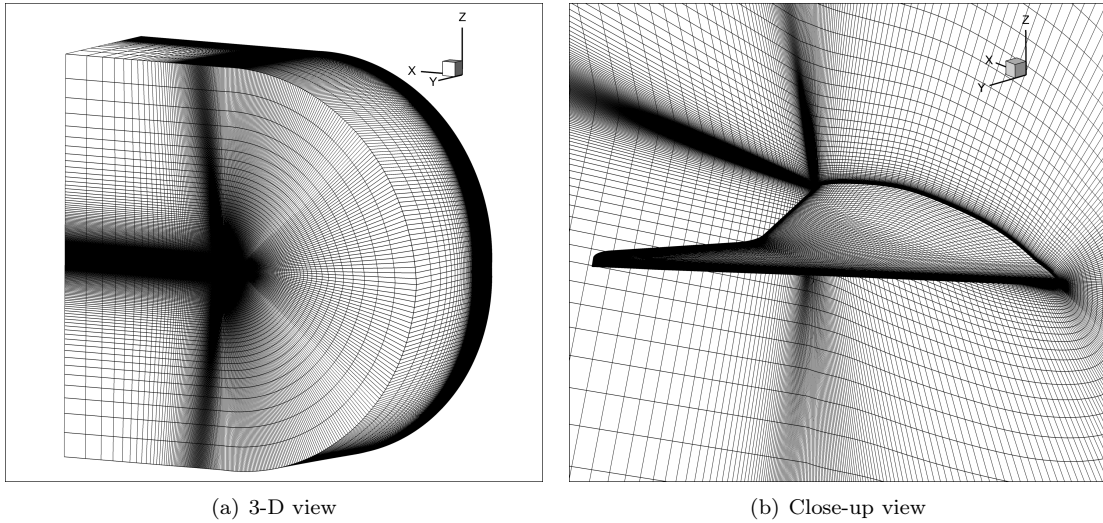


Figure 2: Grid system of the tailless lambda wing model

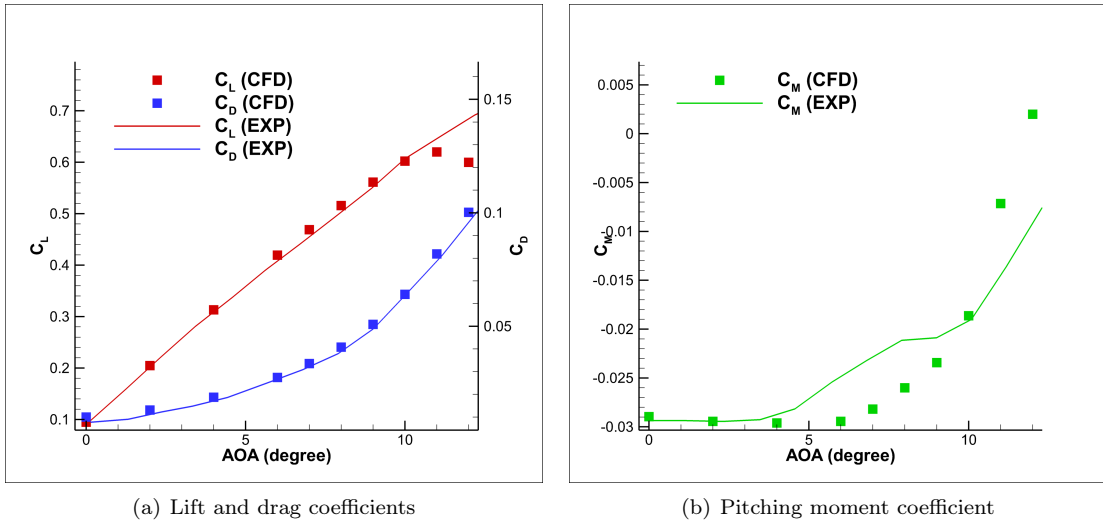


Figure 3: Comparison of aerodynamic coefficient (without VG)

graphs show differences between the numerical results and the experimental results [7] quantitatively, the major flow physics are represented qualitatively well by the numerical simulations.

The parametric study and the design optimization were performed at 11° angle of attack because, at this angle of attack, the separated flow region extends rapidly from the outboard to the inboard with the rapidly rising pitching moment.

2.2 Vortex Generator

A vortex generator (VG) has been used widely to delay the separation on the upper wing and to guide flows on the nacelle for commercial airplanes. The VG is also capable of improving the performance of engine inlets, automobiles, and wind turbine blades. Therefore, many studies have been conducted to analyze the effect of the VG. However, a flow computation using the conventional fully gridded approach requires a large number of computational cells to resolve flows around the VG. To reduce the computational cost while maintaining accuracy, the Bender–Anderson–Yagle (BAY) model [8] was developed to model a lift force of a VG by a mathematical source term. Jirasek [9] developed the jBAY model, which expanded the idea of the

BAY model to an unstructured grid, and Yi *et al.* [10] developed the differentiable BAY model, which is the BAY model improved to be suitable for sensitivity analysis.

2.2.1 BAY Model

As a mathematical source term to model a VG, the BAY model is simply employed to the incompressible Navier–Stokes equation as follows:

$$\Delta V_i \frac{\rho \Delta u_i}{\Delta t} = \sum_j F_M \Delta S + L_i \quad (1)$$

where L_i is the source term representing the lift force of the VG. Equation (1) is the momentum equation. j is the flux summation along the boundary of the i th cell. The source term, L_i can be expressed as follows:

$$L_i = C_{VG} S_{VG} \left(\frac{\Delta V_i}{\sum_j \Delta V_j} \right) \rho |\vec{u}|^2 (\hat{u} \times \hat{b}) (\hat{u} \cdot \hat{n}) (\hat{u} \cdot \hat{t}) \quad (2)$$

where C_{VG} is a relaxation parameter controlling the strength of the lift force, S_{VG} is the VG planform area, ρ is the local density (constant in this case), and \vec{u} is the local velocity. \hat{u} is the unit velocity vector, \hat{b} is the unit vector parallel to the VG (or normal to the body surface), \hat{t} is the unit vector tangent to the VG, and \hat{n} is the unit vector normal to the VG. The geometric definition for VG is presented in Figure 4. ΔV_i is the volume of the i th cell, and $\Delta V_i / \sum_j \Delta V_j$ is the volume ratio of the lift force for the i th cell. These terms related to the volume were modified to be differentiated in the differentiable BAY model.

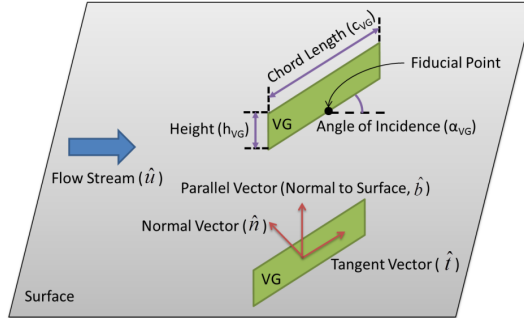


Figure 4: Geometric definitions of VG

2.2.2 Differentiable BAY Model

From the view point of the flow sensitivity for a gradient-based optimization, the original BAY model needs to be modified. Since the original model is formulated with the whole volume of each computational cell crossed by the VG, this model cannot reflect a small amount of positional change within the computational cell. To overcome this limitation, the differentiable BAY model [10] was developed and utilized for the design of multiple VGs. The expression for the lift force is the same as that in the original BAY model, but the volume of the computational cell crossed by the VG was replaced by the overlaid VG volume to take into account small positional changes to achieve flow sensitivity.

3 Parametric Study

Prior to the design optimization, several parametric studies were performed to examine the variation of the flow characteristics according to the geometric and positional parameters of the VG array. To decide the baseline configuration of the VG array for the parametric study and the optimization, positions and the number of VG array were selected through several tests. The VG is a thin-plate type and has 6% of the

MAC in length and 1% of the MAC in height; these sizes were set as the baseline in all the parametric studies.

Firstly, to determine the baseline location of the VG array, several tests were carried out by changing the position of a single VG. The single VG was initially installed near a leading edge, and the spanwise position of the VG was varied from $\eta = 0.388$ to $\eta = 0.808$, including the separated flow region ($\eta > 0.51$). The baseline VG location was then chosen at $\eta = 0.528$, where the reduction effect of the pitching moment coefficient was the most visible.

Next, VGs were installed additionally on either side of the VG fixed at $\eta = 0.528$. VGs were placed side by side, and the space between VGs was set to match the chord length of the VG. When a total of seven VGs were installed, the change of the pitching moment by the VGs was similar to the increased amount of the pitching moment caused by increasing the angle of attack without VGs. Thus, seven VGs were chosen for the baseline for the VG array. For the parametric studies, consequently, the baseline VG array was composed of seven VGs in a line along the swept leading edge.

The parameters used in the parametric studies, their ranges, and a comparison graph are presented for each case, and the result was compared to the case without VGs. Without VGs, which is referred to as the initial case, the pitching moment coefficient at the design condition ($\alpha = 11^\circ$) is -0.00715 . The percentages of the improvement amounts were calculated as follows:

$$\text{Improvement (\%)} = \frac{X_{\text{improved}} - X_{\text{initial}}}{X_{\text{initial}}} \times 100 \quad (3)$$

where X is a value such as the pitching moment coefficient, the total area of the VG array, and so forth.

As a first case, the VG array was installed on the upper wing near the leading edge, and the positional effects of the VG array were checked by moving it toward the trailing edge along the chordwise direction (Case 1). Next, the incidence angle of the VGs was changed to consider effects of the amount of supplied energy and the flow guiding direction (Case 2). For Cases 3 and 4, the space between VGs and the size of VGs were varied to consider the interaction between vortices produced by adjacent VGs.

3.1 Case 1: Changing Chordwise Position of VG Array

As a first parametric study, the flow characteristics related to the boundary layer and the VG array on the upper wing were observed. This VG array moved across the chordwise direction from the leading edge to the trailing edge, as shown in Figure 5. Chordwise positions (x -position) of the fourth VG, located at the center of the array, tested in this parametric study are shown in Table 2.

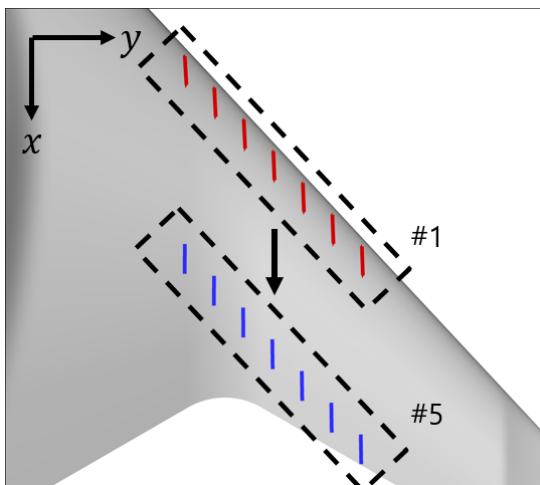


Figure 5: Positional changes of VG array in chordwise direction

Table 2: x positions of the center VG

Location #	x position
1	0.854366
2	0.954366
3	1.054366
4	1.154366
5	1.254366

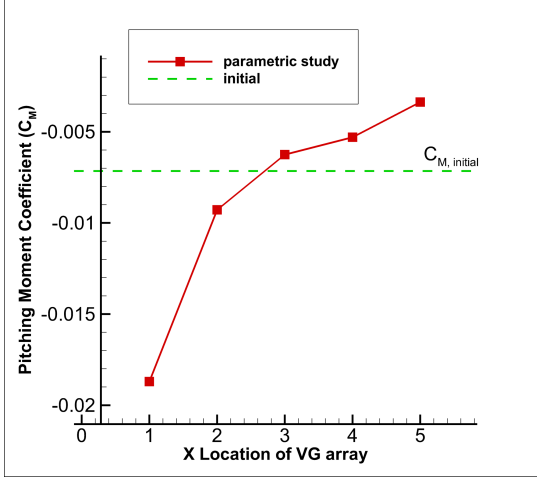


Figure 6: The changes of C_M depend on the x location of VG array

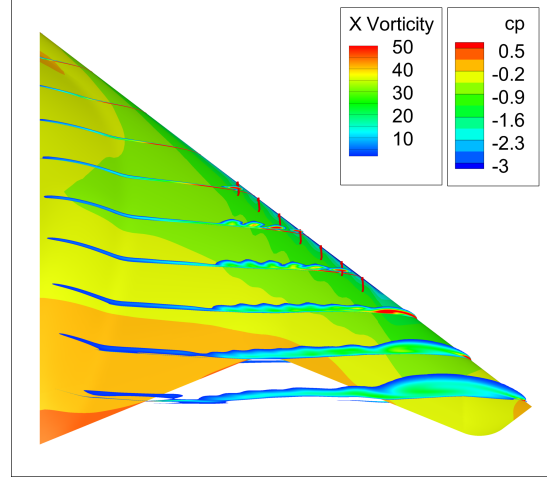
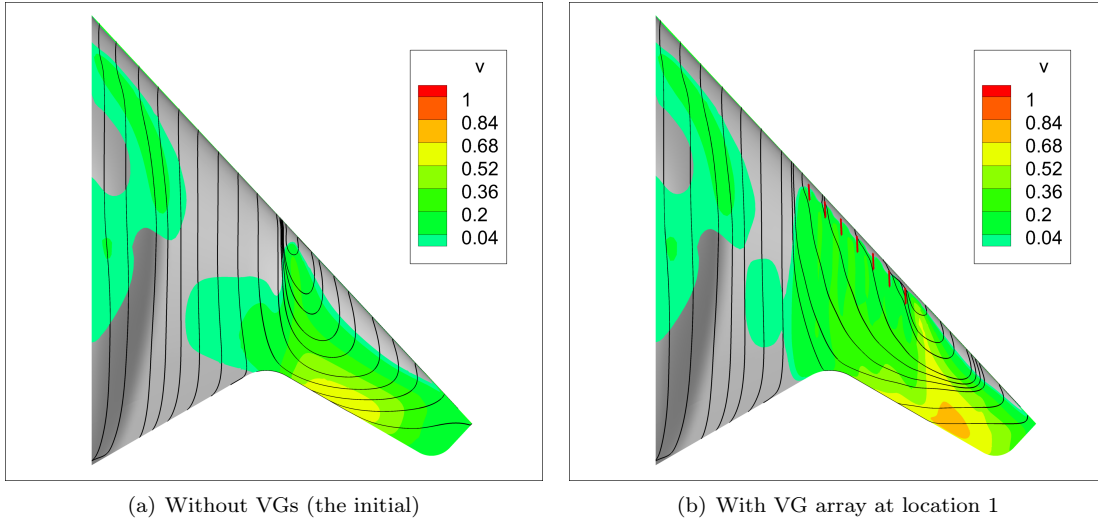


Figure 7: Surface C_p contour and axial vorticity with VG array at location 1



(a) Without VGs (the initial)

(b) With VG array at location 1

Figure 8: Spanwise velocity (v/U_∞) contours and skin friction lines (The gray-colored region denotes the negative velocity, $U_y < 0$)

In the comparison graph (Figure 6), the broken green line is the initial C_M , and the solid red line is the computed result, which is the same in all comparison graphs of all parametric studies. After the installation of the VG array, the pitching moment improved maximally at the front and increased as the VG array moves backward. Behind the middle of the wing in chordwise direction, the pitch-down moment is smaller than the initial value. The maximum improvement of C_M is 162% (from -0.00715 to -0.01870). Although this amount of improvement is quite substantial, a separated flow region still remains around the wing tip as shown in Figure 7.

Figure 8 shows the spanwise velocity (y -velocity) in the boundary layer. As shown in the figure, the vortices produced by the VG array make the spanwise momentum in the boundary layer strong, and the spanwise momentum pushed the separation out to the wing tip. However, when the VG array is located after the middle of the wing, it cannot generate sufficient spanwise momentum and can affect the rear separation region only, so its effect decreased.

3.2 Case 2: Changing Incidence Angle of VGs

As a second parametric study, the flow characteristics related to the strength of vortices produced by VGs and the flow direction turned by VGs were observed. The incidence angle was changed from -20° to 20° at 10° increments, as shown in Figure 9. The incidence angle is 0° when the VG is parallel to the freestream.

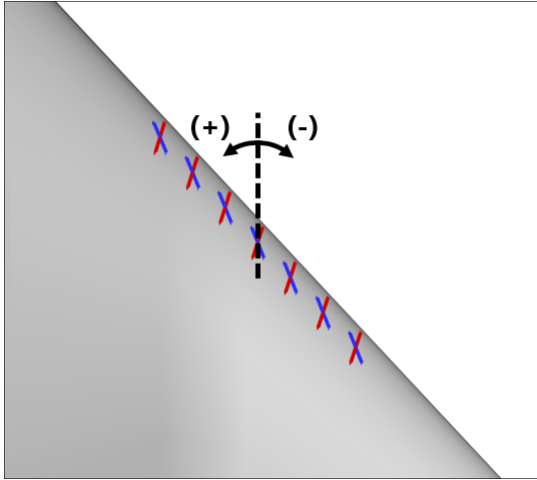


Figure 9: Variations of incidence angle of VG array

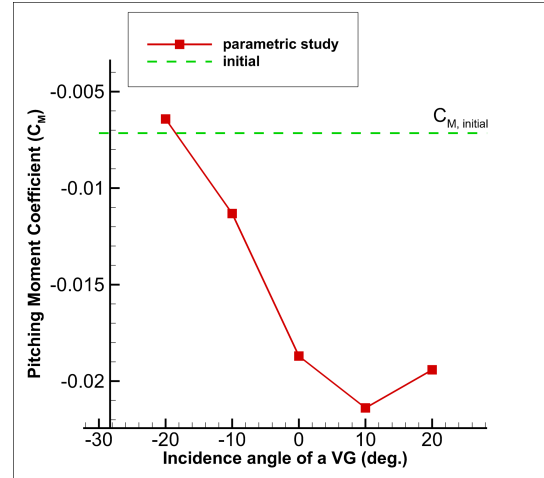


Figure 10: The changes of C_M depend on the incidence angle of VGs

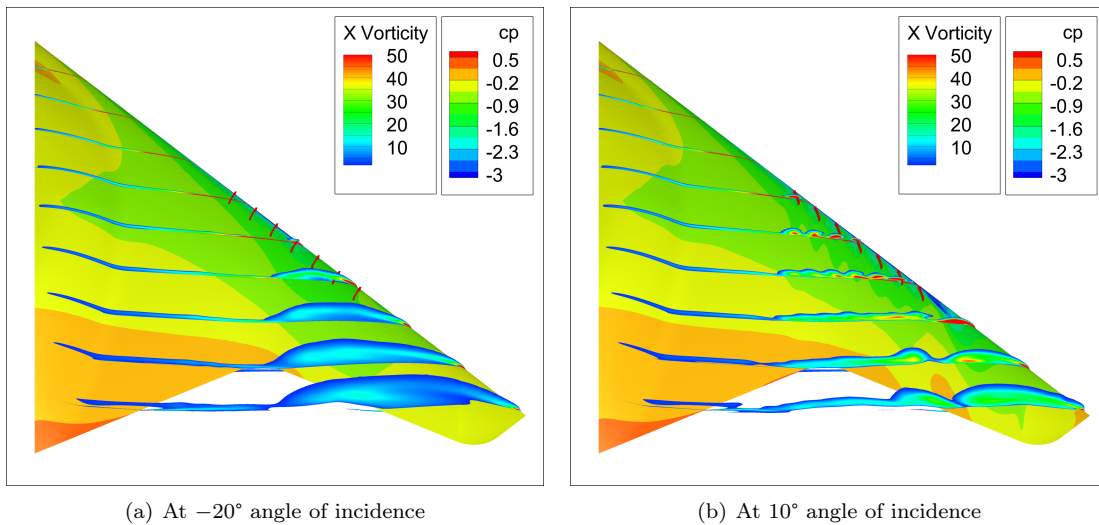


Figure 11: Surface C_p contour and axial vorticity with VG array

Figure 10 shows that all test cases decreased C_M more than the initial value except the angle of -20° . The amount of decrease in C_M grows until the angle of 10° , as VGs are rotated in a counter-clockwise direction until the angle of 10° . After that angle, the trend reverses. The maximum improvement of C_M is 199% (from -0.00715 to -0.02139) at the angle of 10° .

As shown in Figure 11(a), there are no vortices produced by VGs at the angle of -20° , because the local flow direction is not parallel to the freestream. The flow turned inward through the leading edge, and the angle of the local flow is about 20° in clockwise direction.

Positive incidence angle in counter clockwise direction enhanced positive axial vortices produced by VGs, and it enhanced the speed toward the wing tip in the boundary layer before the separated flow region, which is shown in Figure 12. This increased spanwise momentum pushed out the flow separation. Moreover, there

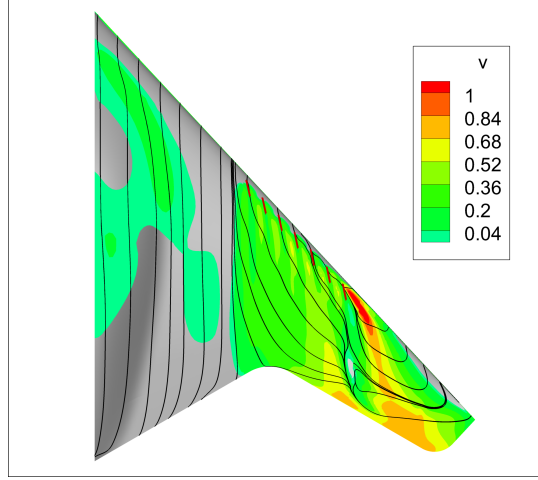


Figure 12: Spanwise velocity (v/U_∞) contours and skin friction lines (The gray-colored region denotes the negative velocity, $U_y < 0$)

are leading edge vortices just behind the VG closest to the wing tip at both angles of 10° and 20° , as shown in Figure 11(b); thus, it produced the suction force, and C_M decreased more than the baseline at these angles of incidence.

3.3 Case 3: Changing Space between VGs

As a third parametric study, the flow characteristics related to the interaction between vortices produced by adjacent VGs were observed by changing space between VGs. The space between VGs was changed from 0.5 to 2.5 times based on the space of the baseline VG array: 0.03, 0.06, 0.09, 0.12, and 0.15, nondimensionalized by the MAC, as shown in Figure 13.

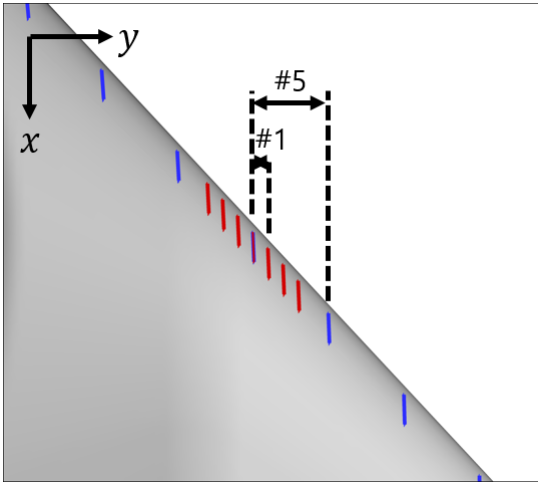


Figure 13: Variations of space between VGs

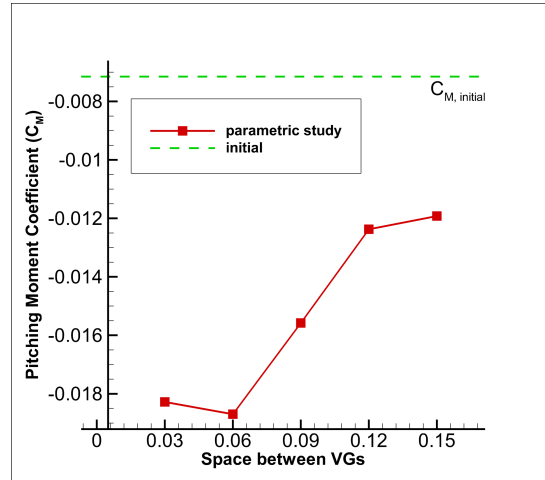


Figure 14: The changes of C_M depend on the space between VGs

Figure 14 shows that all test cases decreased C_M more than the initial case. The amount of C_M decrease declines as the space between VGs widens. The maximally decreased C_M is 162% (from -0.00715 to -0.01870), which is the same as that of Case 1.

When the space between VGs is more than 0.09 (the space is 0.15 in Figure 15(a)), there is more distance to interact between the adjacent vortices; thus, its affect almost similar to the single VG. On the other hand, when the space of VGs is 0.03 (Figure 15(b)), several vortices produced by VG array combined into one

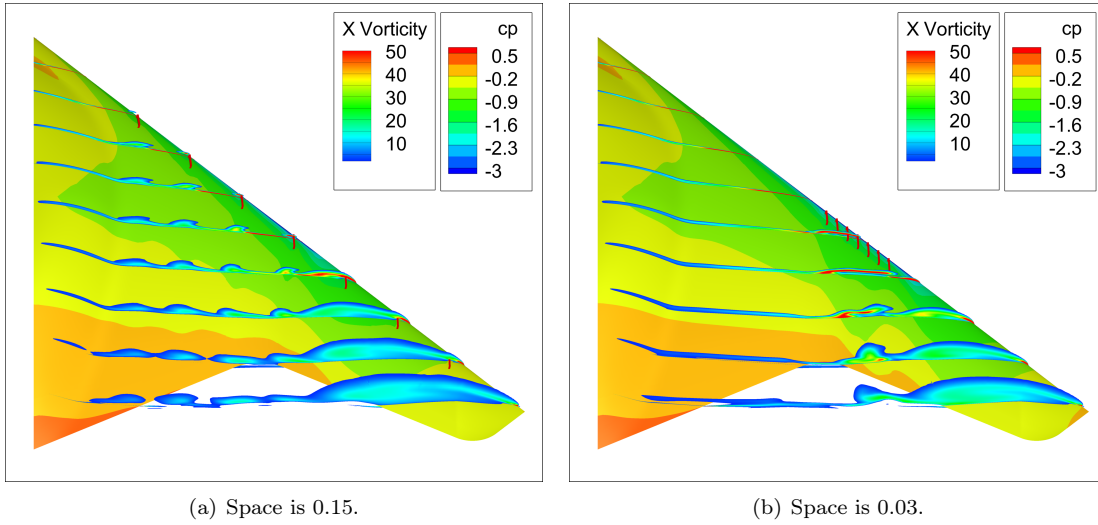


Figure 15: Surface C_p contour and axial vorticity with VG array

vortex as it moved downward. In this case, the interaction effect is maximum when the space is equal to the chord length.

3.4 Case 4: Changing Size of VGs

This parametric study is similar to Case 3, but the size of VGs is changed instead of the space between VGs. The size of VGs was changed from 0.25 to 2.0 times based on the size of the baseline VG array, as shown in Figure 16. The four VGs are illustrated in relative sizes at the top of the figure.

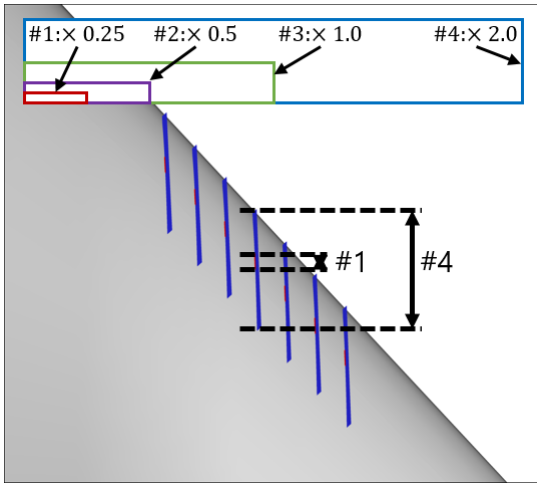


Figure 16: Variations of size of VGs

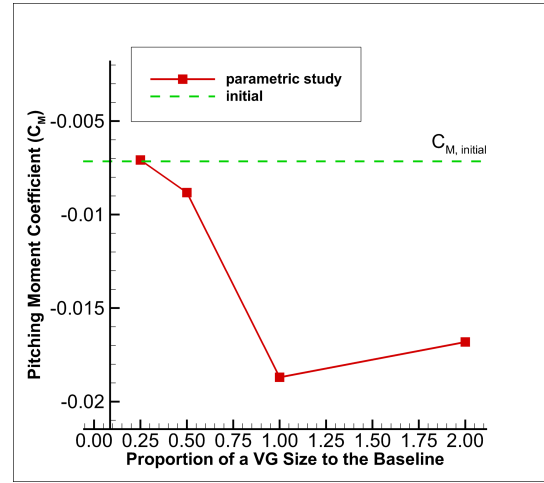


Figure 17: The changes of C_M depend on the proportion of a VG size to the baseline

Figure 17 shows that the baseline exhibits the best performance ($C_M = -0.0187$). When VG size is smaller than the baseline, the effect of VGs weakens rapidly, and there is no effect in the case of the smallest VGs.

When the VG size is 0.5 or 2.0, it shows the same trends as Case 3 of the parametric study, when the space is 0.12 or 0.03, respectively. These are the same ratios in a viewpoint of the ratio of the space to the chord length. As shown in Figure 18, one vortex is merged by vortices with the VG size of 2.0, similar to when the space is 0.03 in the parametric Case 3. If the size proportion is less than 0.5, vortices produced by

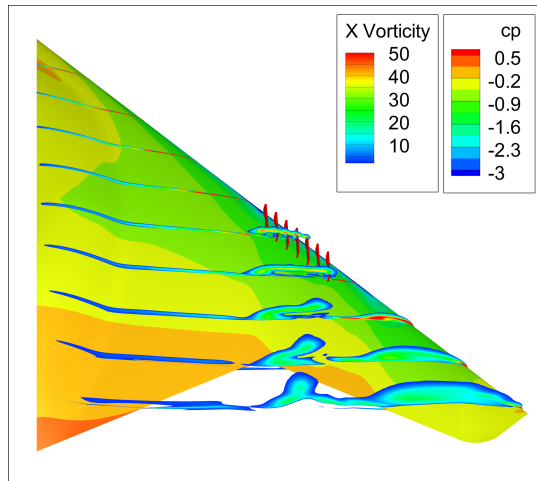


Figure 18: Surface C_p contour and axial vorticity with the VG size of 2.0

VG array is not observed and the separated flow region remained.

3.5 Summary of Parametric Studies

From the results of parametric studies, there are some characteristics related to the control of the separation with a VG array. Firstly, a VG array is possible to mitigate the separation flow with the enhanced spanwise velocity in the boundary layer. The rotation of VGs in toe-in direction strengthens the positive axial vortices and the spanwise velocity. There is the right distance to maximize the interaction between neighboring VGs. In the parametric study, the interaction effect is maximized if the space between VGs is almost equal to the chord length of VG. In addition, there is the proper size because the control effect decreased rapidly as the size decreased.

4 Design Optimization Strategy

Conventionally, the design optimization of a VG configuration is carried out without considering local flow conditions of each VG. This is because it is hard to compute a sensitivity of a VG configuration when a mathematical model such as the BAY model is used. Thus, the design of experiment (DOE) method has been used widely for the design optimization of VGs. To overcome this limitation, Yi *et al.* [10] and Yi and Kim [11] adopted a design approach for VGs by utilizing the advantages of adjoint variable-based approach and the differentiable BAY model. Using this approach, VGs can be independently designed with a large number of design variables, and the designed VGs can fully reflect the local flow characteristics near each VG.

This approach was used for the present design to optimize the shape and position of VGs efficiently. A total of seven VGs could be treated with design variables of chord length, height, incidence angle, streamwise position, and spanwise position of each VG, resulting in 35 design variables in total. Two design optimizations were performed, and the baseline of the optimizations was the same as the baseline of the parametric study described in Section 3.

4.1 Optimization Technique and Objective Function

For the present design of the VG array, a Gradient-Based Optimization Method (GBOM) is used and a discrete adjoint variable method is employed to obtain a sensitivity information. The differentiable BAY model was implemented to describe and calculate the sensitivity of the VG source term model. The Design Optimization Tool (DOT) program was selected as an optimizer, and the search direction was determined by the Broyden-Fletcher-Goldfarb-Shanno (BFGS) method.

In the tailless lambda wing model, the pitch-up results in increasing the pitching moment; thus, decreasing the pitching moment alleviates the pitch-up. In addition, to reduce the slope of the pitching moment coefficient, the objective function had the difference of C_M between 11° , which is the design point, and 6° , which is the onset of the pitch-up. As the VG size increases, it has detrimental effects on aerodynamic performance or observability of the aircraft. For example, drag and Radar Cross Section (RCS) are increased in proportion to an area and a square of an area, respectively. Therefore, the minimization of the total area of VGs was also added to the objective.

The design objective is to minimize the pitching moment coefficient difference and the total area of the VG array simultaneously. Then, the objective function is defined as a weighted sum like the following:

$$F_{\text{obj}} = |C_{M,11^\circ} - C_{M,6^\circ}| + w \cdot \sum_{i=1}^{\text{nVGs}} S_{\text{VG},i} \quad (4)$$

where $C_{M,11^\circ}$ and $C_{M,6^\circ}$ are pitching moment coefficients at 11° and 6° , respectively. w is weighting factor, $S_{\text{VG},i}$ is the area of i th VG, and n is the number of VGs in the VG array. Weighting factor (w) is set as 2.8571 to balance the scale of values between the change of C_M and the total area of VG array.

4.2 Discrete Adjoint Variable Method with Differentiable BAY Model

A discrete adjoint solver developed by fully hand-differentiating 3-D incompressible Navier–Stokes equations coupled with a two-equation turbulence model was applied [10, 12, 13, 14]. The sensitivity of the objective function can be calculated as

$$\left\{ \frac{dF}{dD} \right\} = \left\{ \frac{\partial F}{\partial X} \right\}^T \left\{ \frac{dX}{dD} \right\} + \left\{ \frac{\partial F}{\partial D} \right\} + \Lambda^T \left(\left[\frac{\partial R}{\partial X} \right] \left\{ \frac{dX}{dD} \right\} + \left\{ \frac{\partial R}{\partial D} \right\} \right) \quad (5)$$

where if Λ satisfies the following adjoint equation:

$$\left\{ \frac{\partial F}{\partial Q} \right\}^T + \Lambda^T \left[\frac{\partial R}{\partial Q} \right] = \{0\}^T \quad (6)$$

Because the residual includes the VG source term (L_i), we have

$$\left\{ \frac{\partial R}{\partial D} \right\}^T = \left\{ \frac{\partial}{\partial D} \left(\sum_j \text{Flux} + L_i \right) \right\}^T \quad (7)$$

Finally, the sensitivity of the objective function is calculated as

$$\left\{ \frac{dF}{dD} \right\} = \Lambda^T \left\{ \frac{\partial R}{\partial D} \right\} = \Lambda^T \left\{ \frac{\partial L_i}{\partial D} \right\} \quad (8)$$

because the present objective function (F) is independent of the computational mesh (X), numerical flux (R), and the design variables (D).

4.3 Baseline VG Configuration and Design Range

The results of the parametric study indicate that there exist an optimal size and position to minimize the pitching moment while keeping the total area of VG array as small as possible. As the baseline of the parametric study, VG array composed of 7 VGs side-by-side in spanwise direction were adopted for a baseline configuration of each design case. The design parameters include the chord length (c_{VG}), the height (h_{VG}), the incidence angle (α_{VG}), the chordwise position (x_{VG}), and the spanwise position (y_{VG}) of each VG. Geometric parameters such as chord length, height, and incidence angle are nondimensionalized by the MAC, and positional parameters such as chordwise and spanwise positions are mapped to the planform

domain ($u - v$ coordinates) from the physical domain ($x - y$ coordinates), as shown in Figure 19. The design range and the positions of the baseline VGs are presented in Tables 3 and 4, respectively.

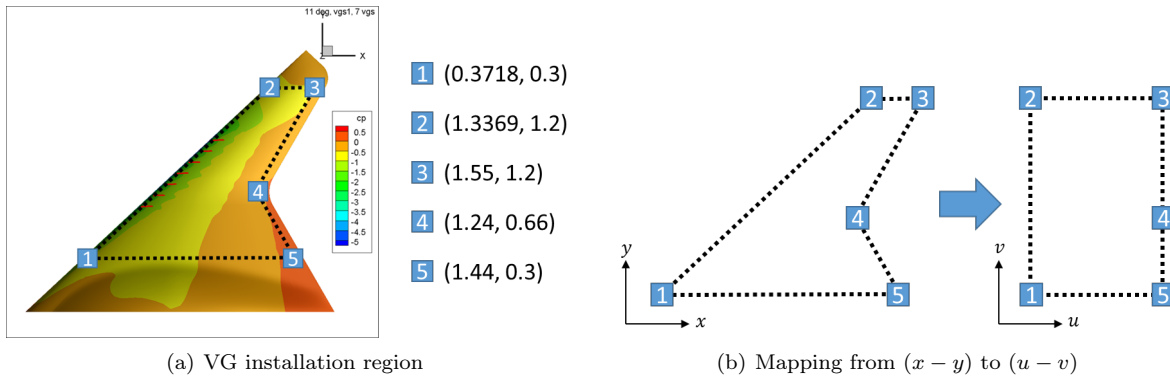


Figure 19: VG installation region and mapping from $(x - y)$ to $(u - v)$

Table 3: The range of design parameters

Design parameter	Lower bound	Initial value	Upper bound
Chord	0.001	0.06	0.12
Height	0.001	0.01	0.02
Angle ($^\circ$)	-45.0	0.0	45.0
x or y positions	$u = 0, v = 0$	-	$u = 1, v = 1$

Table 4: Baseline positions of VGs

VG #	Position (x, y)
VG1	(0.57, 0.661340)
VG2	(0.63, 0.725682)
VG3	(0.69, 0.790024)
VG4	(0.75, 0.854366)
VG5	(0.81, 0.918708)
VG6	(0.87, 0.983050)
VG7	(0.93, 1.047392)

5 Design Result

Two cases of design optimization were performed. The first design case considered all VGs having the same chord length, height, and incidence angle. Position of each VG was considered independently. Seventeen design variables were used. The second design case considered every geometric parameters and positional parameters of each VG independently; thus, 35 design variables were used. The baselines of each design case are the baseline VG array used in the parametric study.

5.1 Design Case 1: Optimizing VGs with Identical Shape

The first design was performed with 17 design variables, treating every VG of the VG array equally. Using the GBOM design process, a designed VG configuration was obtained within 24 design iterations. The number of sensitivity analyses was only three, and the optimized result was obtained through 12 design iterations, which are shown in Figure 20.

The objective function decreased 29.3%, from 0.02178 (baseline) to 0.01541 (designed), as shown in Figure 20. The total area of VG array decreased 41.9%, from 0.00420 (baseline) to 0.00244 (designed). The chord length and the height of each VG are changed from 0.06 and 0.01 normalized by MAC to 0.0466 (-22.3%) and 0.0075 (-25.1%) normalized by MAC, respectively.

The C_M decreases from -0.01870 (baseline) to -0.02012 (designed), and the performance is improved 181.6% from the initial case (without VGs). Both C_L and C_D improved together, showing 6.8% increase and 8.1% decrease, respectively. The lift coefficient increased from 0.61996 (without VG) and 0.66141 (baseline) to 0.66206 (designed), and the drag coefficient decreased from 0.08189 (without VG) and 0.07455 (baseline)

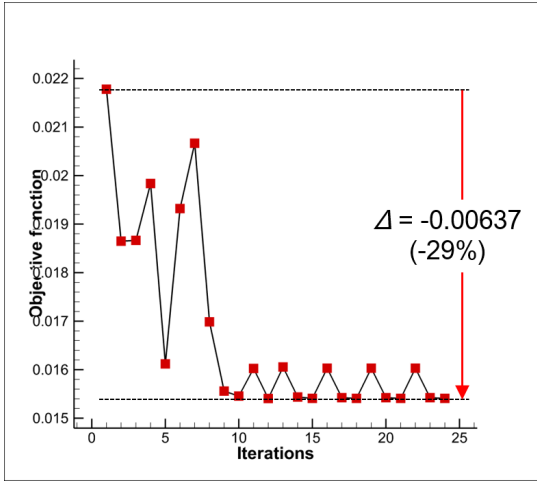


Figure 20: Design history of objective function

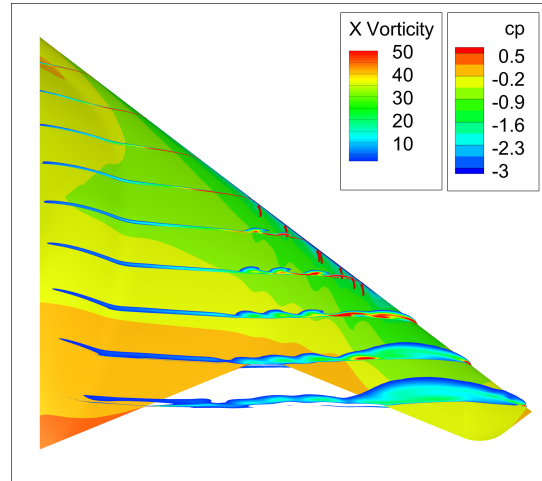


Figure 21: Surface C_p contour and axial vorticity with the designed VG array

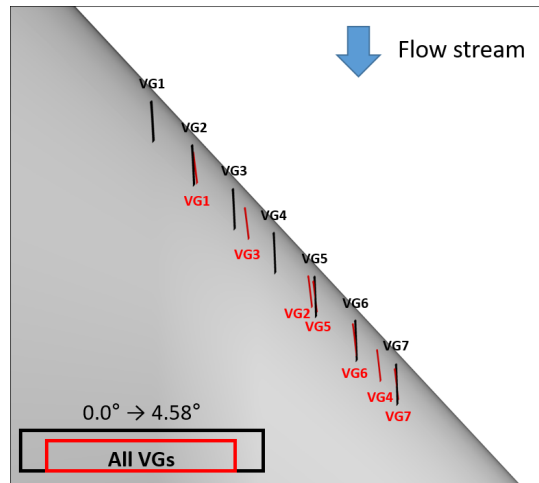


Figure 22: Designed VGs, and their shapes and positions

to 0.07524 (designed). From the viewpoint of the portion of the lift and drag, the pressure portion of lift and drag were improved, while the viscous portion was almost maintained.

Shapes and positions of VGs are shown in Figure 22. In the figure, the VG arrays before and after the design optimization are shown in black and red, respectively, which is the same in all figures for shapes and positions of VGs. Every VG moved to the wing tip except for VG5, VG6, and VG7, which are close to the wing tip, and their positions were maintained. VG2 and VG4 moved to a distant location in spanwise direction. VG2 was located beside VG5. VG4 was located between VG6 and VG7. To maintain the effect of the baseline VG array with the smaller VGs, they were rotated 4.58° counter-clockwise to strengthen vortices and spanwise momentum.

As shown in Figure 21, there is a stronger vortex (higher x -vorticity) than others just before the separated flow region. It seems to be made by interaction with vortices generated by VG4, VG6, and VG7, and it hinders the separation as a fence.

5.2 Design Case 2: Optimizing VGs with Individual Shapes

The second design was conducted with 35 design variables with respect to the VGs. The total number of design iteration was 36, and the number of sensitivity analyses was seven. The optimized result was obtained

at 27 design iterations, and the history of the objective function is shown in Figure 23.

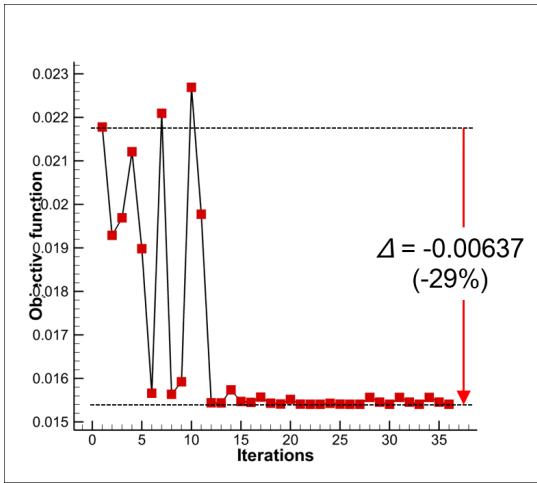


Figure 23: Design history of objective function

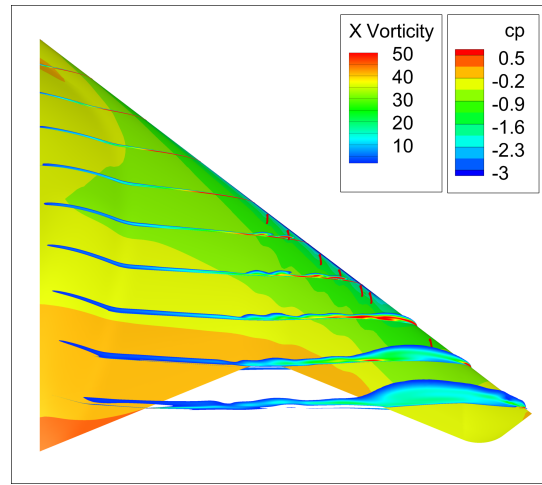


Figure 24: Surface C_p contour and axial vorticity with the designed VG array

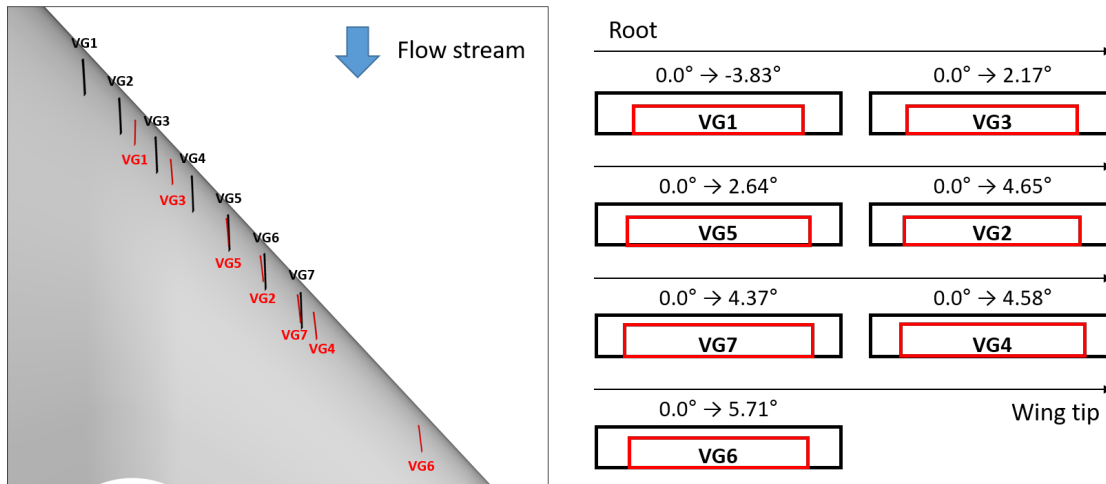


Figure 25: Designed VGs, and their shapes and positions

Table 5: Chord length, height, and incidence angle of the designed VGs (sorted from root to wing tip)

VG #	Chord length	Height	Incidence angle
1	0.0416 (-30.6%)	0.0068 (-32.1%)	-3.84°
3	0.0418 (-30.3%)	0.0068 (-32.5%)	2.17°
5	0.0449 (-25.1%)	0.0069 (-31.1%)	2.64°
2	0.0432 (-28.1%)	0.0068 (-31.6%)	4.65°
7	0.0462 (-23.0%)	0.0077 (-23.4%)	4.37°
4	0.0453 (-24.5%)	0.0078 (-22.0%)	4.58°
6	0.0439 (-26.8%)	0.0072 (-28.3%)	5.71°

The objective function decreased 29.3%, from 0.02178 (baseline) to 0.01541 (designed), as shown in Figure 23. The total area of VG array decreased 47.8%, from 0.00420 (baseline) to 0.00219 (designed). The size of each VG decreased average 27%. The changes of the chord length and the height of each VG, and their percentage change from the baseline VGs are shown in Table 5, and they are nondimensionalized by MAC.

The optimized C_M is almost the same as in Design Case 1, which changed from -0.01870 (baseline) to -0.01944 (designed). Both C_L and C_D also improved together, as in Design Case 1, amounting to 6.5% and 9.6%, respectively. The lift coefficient increased from 0.61996 (without VG) and 0.66141 (baseline) to 0.66000 (designed), and the drag coefficient decreased from 0.08189 (without VG) and 0.07524 (baseline) to 0.07404 (designed).

The changing pattern of the shape and the position of each VG is illustrated in Figure 25. For convenience, the orders of VGs are sorted from root to wing tip by y -positions of VGs. All VGs were rotated counter-clockwise except for VG1, located at the innermost side, which was rotated clockwise. The incidence angle of VGs tended to increase from -3.83° at the innermost to 5.71° at the outermost. The size of VGs, except for VG6 located at the outermost, tended to enlarge gradually from the innermost to the outermost also. Similar to Design Case 1, VGs moved to the wing tip except for VG5 and VG7, the positions of which were maintained. VG2 replaced VG6, and VG4 moved to behind VG7. VG6 moved far away to outboard of the wing, and it was trapped inside the separated flow.

The region of separated flow and the surface pressure contour are illustrated in Figure 24. The separated flow region is diminished with the designed VG array also. To push the separation region out effectively, VGs were rotating to toe-in and increasing while going near to the separation region. In addition, vortices generated by VG4 and VG7, located just before the separation region, were combined and strengthened, similar to Design Case 1. VG6 was located inside the separation, thus it was hard to play a role and delay the separation.

5.3 Summary of Design Optimization

Both of the designed VG arrays showed considerable improvement compared to before the VG installation, even if the separated flow region was not eliminated totally. All of the optimized VG arrays made the separated flow region diminished, thereby expanding the suction region behind the MRP, and this decreased pitching moment. Both the lift and drag performance were improved by an alleviation of a separation similar to an airfoil when the separation was suppressed.

The off-design performances of these optimized VG arrays were examined by changing the angle of attack, and the results are plotted as illustrated in Figure 26.

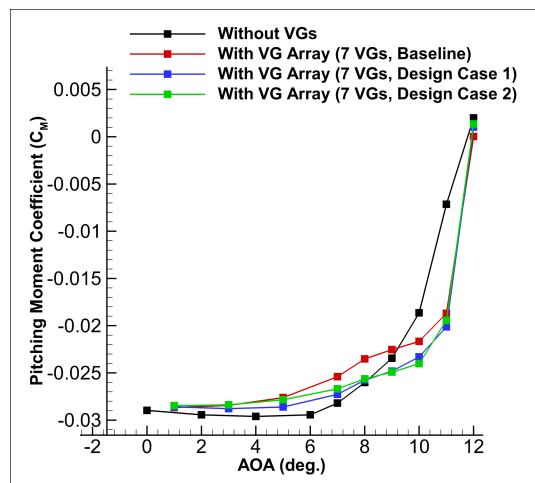


Figure 26: Comparison of pitching moment coefficients

Results show a greater reduction under 11° angle of attack, compared to the case without VG and with the baseline VG array. All graphs increased slope after the 6° angle of attack, but both slopes of each of the two optimizations are smaller than the initial and the baseline. After the design optimization, the designed VG array makes an overall slope gently up to the design condition. However, after the design condition, at 12° angle of attack, VG array has no control effect because the VG array is entirely covered by the separated flow. This brings up the necessity of multi-point optimization to consider the higher angle of attack.

6 Conclusion and Future Work

The present study conducted the design optimization of VG configurations to alleviate the pitch-up on the tailless lambda wing aircraft with the 1303 UCAV planform. The optimization is performed to minimize the pitching moment coefficient while minimizing the total area of VG array, in order to avoid the detrimental effects on the aerodynamic performance or the observability.

For the baseline of the optimization, the VG array was constituted by seven VGs forming a row along the leading edge. Each VG was optimized individually by fully reflecting the local flow pattern with 5 design parameters. To handle a large number of design variables, the discrete adjoint variable method with the differentiable BAY model was adopted for the sensitivity analysis.

Before the design optimization, four cases of parametric study were performed to identify trend with respect to the chordwise position, incidence angle, space between VGs, and size of VG. After the parametric study, the optimizations of the VG array configuration were conducted, and VGs pushed out and diminished the separation region successfully, but did not totally eliminate the flow separation. The chord length and the height of VGs reduced over an average of 23%, and the total area of VGs decreased over 42%. Pitching moment decreased over 4% (from the baseline) and 170% (from the initial), and both the lift and drag performance were improved.

At off-design conditions, the C_M improvement is visible up to 11° angle of attack, which is the design condition. Subsequently, however, the designed VG array has no control effect because the separation region expands to a large extent over the VGs. Considering the lower angle of attack and the higher angle of attack simultaneously, the performance of the VG array at the off-design conditions could be improved.

Acknowledgement

This work was supported by the Advanced Research Center Program (NRF-2013R1A5A1073861) through the National Research Foundation of Korea grant funded by the Korea government contracted through the Advanced Space Propulsion Research Center at Seoul National University, and by the KISTI Supercomputing Center (KSC-2017-C3-0071).

References

- [1] M. T. Arthur and K. Petterson. A Computational Study of the Low-speed Flow over the 1303 UCAV Configuration. In *25th AIAA Applied Aerodynamics Conference*, 2007.
- [2] M. D. Wong, G. J. McKenzie, M. V. Ol, K. Petterson, and S. Zhang. Joint TTCP CFD Studies into the 1303 UCAV Performance: First Year Results. In *24th Applied Aerodynamics Conference*, 2006.
- [3] S. C. McParlin, R. J. Bruce, A. G. Hepworth, and A. J. Rae. Low Speed Wind Tunnel Tests on the 1303 UCAV Concept. In *24th Applied Aerodynamics Conference*, 2006.
- [4] M. V. Ol. Water Tunnel Velocimetry Results for the 1303 UCAV Configuration. In *24th Applied Aerodynamics Conference*, 2006.
- [5] S. Yoon and A. Jameson. Lower-upper Symmetric-Gauss-Seidel method for the Euler and Navier-Stokes equations. *AIAA Journal*, 26(9):1025–1026, 1988.
- [6] F. R. Menter. Two-Equation Eddy-Viscosity Turbulence Models for Engineering Applications. *AIAA Journal*, 32(8), 1994.
- [7] H. J. Shim, S. O. Park, and S. Y. Oh. An Experimental Study on Aerodynamic Coefficients of a Tailless BWB UCAV. In *KSAS Spring Conference*, 2013.
- [8] E. E. Bender, B. H. Anderson, and P. J. Yagle. Vortex Generator Modeling for Navier-Stokes Codes. In *3rd joint ASME/JSME Fluids Engineering Conference*, 1999.
- [9] A. Jirasek. Vortex-Generator Model and Its Application to Flow Control. *Journal of Aircraft*, 42(6):1486–1491, 2005.
- [10] J. Yi, C. Kim, and B. J. Lee. Adjoint-Based Design Optimization of Vortex Generator in an S-Shaped Subsonic Inlet. *AIAA Journal*, 50(11):2492–2507, 2012.
- [11] J. Yi and C. Kim. Design Optimization of Vortex Generators for a Junction Vortex of Wing-Body

Configuration by Discrete Adjoint Approach. *51st AIAA Aerospace Sciences Meeting including the New Horizons Forum and Aerospace Exposition*, 2013.

- [12] B. J. Lee and C. Kim. Aerodynamic Redesign Using Discrete Adjoint Approach on Overset Mesh System. *Journal of Aircraft*, 45(5):1643–1653, 2008.
- [13] C. S. Kim, C. Kim, and O. H. Rho. Sensitivity Analysis for the Navier-Stokes Equations with Two-Equation Turbulence Models. *AIAA Journal*, 39(5):838–845, 2001.
- [14] J. Yim, B. J. Lee, and C. Kim. Exploring Multi-stage Shape Optimization Strategy of Multi-body Geometries Using Kriging-based Model and Adjoint Method. *Computers and Fluids*, 68:71–87, 2012.